Smart Structures and Systems, *Vol. 29, No. 4 (2022) 599-616*
https://doi.org/10.12989/sss.2022.29.4.599

A data fusion method for bridge displacement reconstruction based on LSTM networks

Da-You Duan [1a], Zuo-Cai Wang*[1,2], Xiao-Tong Sun [1b] and Yu Xin [1,3c]

[1] *School of Civil and Hydraulic Engineering, Hefei University of Technology, Hefei, China*
[2] *Anhui Engineering Technology Research Center for Civil Engineering Disaster Prevention and Mitigation, Hefei, China*
[3] *Anhui Engineering Laboratory for Infrastructural Safety Inspection and Monitoring, Hefei, China*

(*Received September 3, 2021, Revised December 11, 2021, Accepted December 15, 2021*)

Abstract. Bridge displacement contains vital information for bridge condition and performance. Due to the limits of direct displacement measurement methods, the indirect displacement reconstruction methods based on the strain or acceleration data are also developed in engineering applications. There are still some deficiencies of the displacement reconstruction methods based on strain or acceleration in practice. This paper proposed a novel method based on long short-term memory (LSTM) networks to reconstruct the bridge dynamic displacements with the strain and acceleration data source. The LSTM networks with three hidden layers are utilized to map the relationships between the measured responses and the bridge displacement. To achieve the data fusion, the input strain and acceleration data need to be preprocessed by normalization and then the corresponding dynamic displacement responses can be reconstructed by the LSTM networks. In the numerical simulation, the errors of the displacement reconstruction are below 9% for different load cases, and the proposed method is robust when the input strain and acceleration data contains additive noise. The hyper-parameter effect is analyzed and the displacement reconstruction accuracies of different machine learning methods are compared. For experimental verification, the errors are below 6% for the simply supported beam and continuous beam cases. Both the numerical and experimental results indicate that the proposed data fusion method can accurately reconstruct the displacement.

Keywords: data fusion; displacement reconstruction; bridge monitoring; long-short term memory networks

1. Introduction

The vertical displacement is an important parameter for bridge structure monitoring, as well as an important index for bridge safety evaluation. The bridge displacement can be measured directly and indirectly. For instance, the leveling system can measure the static bridge displacement directly. For dynamic displacement measurement, there are also many direct measurement methods like linear variable differential transformer (LVDT), real-time kinematic global positioning system (RTK-GPS), laser Doppler vibrometer (LDV), light detection and ranging (LiDAR) (Lee *et al*. 2019), and vision-based system (Ni *et al*. 2019). Measurement with LVDT usually requires a stable reference platform at the measuring location (Moreu *et al*. 2015). Although RTK-GPS devices have been widely used in structural monitoring (Moschas and Stiros 2011), this method is still not accurate enough for bridge dynamic displacement measurement due to the low sampling rate (Kim *et al*. 2018). The laser Doppler vibrometer (LDV) is adopted primarily to measure the vibration characteristics in an optical nonintrusive and remote way (Halil *et al*. 2016). LiDAR and vision-based system methods are susceptible to environmental disturbances. These direct measure methods have limits such as high equipment cost, low sampling rate, and limited applicability.

To ensure the safety and durability of the bridge structure, structure health monitoring (SHM) systems are widely applied to bridges (Jang *et al*. 2010, Yi *et al*. 2013), and the monitoring systems that already exist can assist to monitor the dynamic bridge displacement. Using the SHM data such as strain, acceleration, inclination and GPS data to reconstruct the bridge displacement does not need extra instruments and cost. The displacement reconstruction using the measured strain are mostly based on modal superposition or the curvature fitting. The accuracy of the methods is strongly influenced by the modal measurement and the boundary condition. With distributed fiber Bragg grating sensors, the beam shapes can be estimated using the displacement–strain transformation (Kim *et al*. 2011). The strain-based method is also used by many other researchers (Chung *et al*. 2008, Glaser *et al*. 2012, Kang *et al*. 2007, Rapp *et al*. 2009) to predict the displacement. As for the displacement reconstruction based on acceleration, the accuracy is influenced by the low-frequency noise. Accelerometers can be used as a tool to indirectly measure displacement by the double integration of acceleration (Li *et al*. 2020). Normally baseline correction or high-pass filtering techniques are needed to correct the low-frequency

*Corresponding author, Ph.D., Professor,
E-mail: wangzuocai@hfut.edu.cn
[a] Ph.D. Student, E-mail: duandayou@mail.hfut.edu.cn
[b] Ph.D. Student, E-mail: 2019110563@mail.hfut.edu.cn
[c] Ph.D., E-mail: 2020800133@hfut.edu.cn

ISSN: 1738-1584 (Print), 1738-1991 (Online)

drift error in displacement reconstruction based on the acceleration data (Hester *et al*. 2017). However, the accuracy of displacement obtained from double integration of the acceleration in time history could be undermined by accumulated errors during the integration process (Smyth and Wu 2007, Thong *et al*. 2004). This type of error can be partially corrected by high-pass filters that eliminate low-frequency components (Cho *et al*. 2015, Hoag *et al*. 2017). However, it is still a challenging issue to differentiate the true signal with noise in the time series.

The strain sensors have a relatively low sampling rate comparing to the accelerometers. Using an artificial neural network, Moon *et al*. (2019) suggested a method to predict bridge displacements from strains. When it comes to the high-frequency displacement reconstruction, the sampling rate of the strain measurement is usually not satisfied. Based on data fusion, the displacements of the structure can be reconstructed by multi-source measurements with different sampling rates. The Kalman filter combined with data fusion provides a practical and efficient state estimation approach (Lei *et al*. 2013, Liu *et al*. 2016). In addition, Kim *et al*. (2018) proposed a data fusion method to estimate the structural displacement based on the Kalman filter. Zheng *et al*. (2019) created a data fusion method for dynamic displacement estimation based on a multi-rate Kalman filter.

The machine learning algorithms are able to build the relationships between input and output data automatically, and the algorithms show outstanding robustness and accuracy in the dynamic response reconstruction of bridge structures (Fan *et al*. 2019, 2020, 2021). In this paper, a novel data fusion method is proposed to eliminate the errors coming with the process of displacement reconstruction from strain or acceleration responses. The proposed method is based on long short-term memory (LSTM) (Graves 2012) recurrent neural network (RNN) which can learn how to map the relationships among multivariate time series data from the network training. A network model with three hidden LSTM layers is built first. The dynamic strain, acceleration and displacement responses collected for the network training and displacement reconstruction validation need to be preprocessed by normalization to stabilize the processes and reduce the epochs of the network training. With the training data, the weights of the proposed LSTM network model are trained and updated by the error function. Then, the proposed network can reconstruct the dynamic displacement responses with the strain and acceleration input data. In the numerical simulation, the hyper-parameters influence of the LSTM network is discussed, and the errors of different machine learning methods are compared. To verify the robustness of the proposed method when the strain and acceleration data contain measuring noise, the displacement reconstruction accuracy with different noise level is analyzed. To further evaluate the performance of the proposed method, the experimental verifications of a simply supported beam and a continuous bean are studied. Both the numerical simulation and experimental results indicate that the proposed displacement reconstruction method based on strain and acceleration is of high accuracy and robust to the measuring noise.

2. Theory and method

The data fusion approach is an effective way to eliminate the shortcomings of the strain-or acceleration-based only methods. The machine learning algorithms can achieve data fusion and build the relationship between different kinds of input data and target data (Ma *et al*. 2021). In this paper, a novel data fusion method is proposed to reconstruct the deformation with LSTM networks. The proposed method takes advantage of the high-frequency part of the accelerations and eliminates the error of the strain modal superposition methods coming with mode shape estimation. The LSTM network can be trained with a small training set and the reconstructed displacement is of high accuracy. This method has the advantages as follows: (1) the mode shape and neutral axis are not needed in the deformation reconstruction; (2) the relationships of different kinds of data are mapped by the LSTM network automatically; (3) the accuracy of the displacement reconstruction is improved comparing to the strain-based and acceleration-based method.

2.1 LSTM network

The LSTM network was invented as an improved recurrent neural network (RNN) architecture (Hochreiter and Schmidhuber 1997), and it is widely used in time series modeling (Karim *et al*. 2019, Tian *et al*. 2020, Candon *et al*. 2020). The LSTM networks are designed with the feature to remember the information for a relatively long period. They can not only extract information from a single data point but also the entire series of data.

The LSTM networks are built to reconstruct the bridge displacement which contains the input layer, hidden LSTM layers, and output layer. The stacked LSTM network loops allowing information to persist are presented in Fig. 1. The additional hidden LSTM layers accept the learned representations from prior layers and create the new abstractive representations which can achieve higher accuracy in the displacement reconstruction. The relationship between the input and target time series data can be described accurately due to the depth of the neural network. The input and output data at time t are expressed as

$$\boldsymbol{x}_t = [x_t^1, x_t^2, \dots, x_t^m]^T \qquad \boldsymbol{y}_t = [y_t^1, y_t^2, \dots, y_t^n]^T \tag{1}$$

where m and n denote the number of the input and output data channels respectively. The hidden state vectors $\boldsymbol{h}$ and $\boldsymbol{C}$ are updated and shared in the same layer.

The LSTM networks contain a chain-like structure, and the basic unit of the network is the cell where the data are processed. The details of the internal LSTM cell structure are presented in Fig. 2.

In the LSTM cell, the function σ and *tanh* can be expressed as

$$\sigma(x) = \frac{1}{1+e^{-x}} \tag{2}$$

$$tanh(x) = \frac{e^{x}-e^{-x}}{e^{x}+e^{-x}}. \tag{3}$$

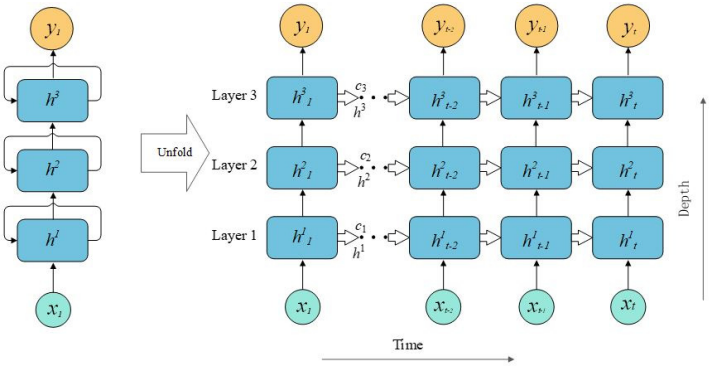

Fig. 1 The loops of the stacked LSTM network

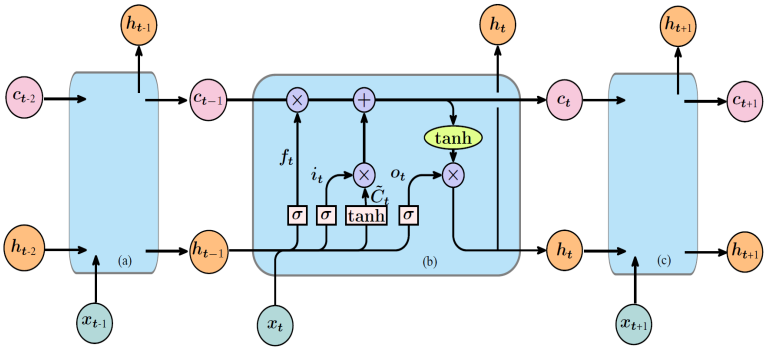

Fig. 2 The repeating cell of the LSTM networks

There are three gates in the cell, which are forget gate, input gate and output gate. The gates control the information into and out of the cell. The forget gate determines how much of the state $\boldsymbol{C}_{t-1}$ to reserve from the last moment by Eq. (4).

$$f_t = \sigma\left(\boldsymbol{W}_f[\boldsymbol{h}_{t-1}, \boldsymbol{x}_t] + \boldsymbol{b}_f\right) \tag{4}$$

where $[\boldsymbol{h}_{t-1}, \boldsymbol{x}_t]$ is the concatenation operation of the vectors $\boldsymbol{h}_{t-1}$ and $\boldsymbol{x}_t$; $\boldsymbol{W}_f$ and $\boldsymbol{b}_f$ are the weight and bias of forget gate f.

The input gate determines the input saved into the $\boldsymbol{C}_t$ by Eq. (5).

$$i_t = \sigma(\boldsymbol{W}_i[\boldsymbol{h}_{t-1}, \boldsymbol{x}_t] + \boldsymbol{b}_i) \tag{5}$$

The output gate controls the output by Eq. (6).

$$o_t = \sigma(\boldsymbol{W}_o[\boldsymbol{h}_{t-1}, \boldsymbol{x}_t] + \boldsymbol{b}_o) \tag{6}$$

The functions of the input and output gates are similar to the forget gate function. The vectors $\boldsymbol{W}_i$, $\boldsymbol{b}_i$, $\boldsymbol{W}_o$, and $\boldsymbol{b}_o$ are the weight and bias of the input and output gates. The candidate cell state $\widetilde{\boldsymbol{C}}_t$ is calculated by Eq. (7) where $\boldsymbol{W}_C$ and $\boldsymbol{b}_C$ are the weight and bias of the cell state. The output $\boldsymbol{h}_t$ of the cell is obtained by Eq. (8) where · represents the dot ·production. In Eq. (9), the $\boldsymbol{C}_t$ is the cell state at time t which is updated by the last cell state $\boldsymbol{C}_{t-1}$ and candidate cell state $\widetilde{\boldsymbol{C}}_t$.

$$\widetilde{\boldsymbol{C}}_t = \tanh(\boldsymbol{W}_C[\boldsymbol{h}_{t-1}, \boldsymbol{x}_t] + \boldsymbol{b}_C) \tag{7}$$

$$\boldsymbol{h}_t = o_t \cdot tanh(\boldsymbol{C}_t) \tag{8}$$

$$\boldsymbol{C}_t = f_t \boldsymbol{C}_{t-1} + i_t \widetilde{\boldsymbol{C}}_t \tag{9}$$

In the training process, the network model gives the estimation forward and the error values are back-propagated from outputs. The gradient of each weight is calculated according to the error. The Adam optimization algorithm (Kingma and Ba 2014) is used to update the weight vectors. The Adam algorithm can calculate the adaptive learning rate for different parameters and occupies fewer storage resources, which is an efficient gradient-based optimization method. According to the Adam algorithm, the weight vector at time t ($\boldsymbol{w}_t$) is updated by the following function

$$\boldsymbol{w}_t = \boldsymbol{w}_{t-1} - \widehat{m}_t \left(\frac{\alpha}{\sqrt{\widehat{v}_t} + \varepsilon} \right) \tag{10}$$

Where the bias-corrected weight parameters $\widehat{m}_t$ and $\widehat{v}_t$, the learning rate α and a small constant ε ($\varepsilon = 10^{-8}$) are used to generate the new weight $\boldsymbol{w}_t$.

The performance of the LSTM network model is evaluated by the root mean square error (RMSE) function which is defined as

$$\text{RMSE} = \sqrt{\frac{1}{k}\sum_{t=1}^{k}(y_t - \hat{y}_t)^2} \tag{11}$$

To further quantify the error between the estimated value and the reference value, the error index E is defined as

$$E = \frac{k \cdot \mathrm{RMSE}}{\sum_{t=1}^{k} \sqrt{(y_t)^2}} \tag{12}$$

where y_t and $\hat{y}_t$ are the target value and the estimated value at time t. k represents the sample volume for the error calculation.

2.2 Bridge displacement reconstruction

To achieve better training performance of the network, the data are prepossessed before being put into the LSTM network. The input data with different units are in different ranges, which may cause the network difficult to converge in the training process. To make the weights of different kinds of data equal, the input and output data are normalized as

$$\begin{aligned} x_t^i &= \frac{\tilde{x}_t^i}{\max\left(\tilde{x}_j^i \mid j = 1 \ldots k\right)}, \qquad i = 1, \ldots m \\ y_t^i &= \frac{\tilde{y}_t^i}{\max\left(\tilde{y}_j^i \mid j = 1 \ldots k\right)}, \qquad i = 1, \ldots n \end{aligned} \tag{13}$$

where $\tilde{x}_t^i$ and $\tilde{y}_t^i$ are the raw input and target data at time t, and x_t^i and y_t^i are the corresponding data after normalization. k represents the number of the data in the sample sires, m and n are the channel of the input and output data, respectively.

The whole process is presented in Fig. 3. The training set and validation set are prepared for LSTM network training. Then the network is trained with the RMSE loss function and the Adam optimization algorithm. After several training epochs, the training and validation losses tend to be constant. If the errors do meet the expectation, the training process will be modified with the learning rate, activation function, batch size, etc. Once the LSTM network is tuned at its best performance, the hidden parameters of the network will be saved. With the preprocessed input data and the trained LSTM network, the output data are obtained. Finally, the reconstructed displacements of the bridge can be concluded by the corresponding normalization factors.

3. Numerical model and simulation

In this section, the finite element model of a steel-concrete composite girder bridge and vehicle models are established. Based on the survey of the traffic flow, the stochastic vehicle flow is generated. With the software Universal Mechanism, the vehicle-bridge coupled system model is established and the bridge responses due to the stochastic vehicle flow are calculated to build the data sets for the LSTM network.

3.1 Bridge model

The bridge finite element model is established based on a Huaihe river bridge in China as shown in Fig. 4. The bridge is a four spans continuous steel-concrete composite girder bridge with 35 m span length. C40 reinforced concrete is used for the bridge deck. The deck thickness is 0.235 m, and the width is 12.4 m. The I-beam girders are made of Q345D carbon structural steel with a spacing of 6.65 m. The cross-section of the bridge is illustrated in Fig. 5. The transverse diaphragms are set for every 5 meters between the two girders. The Young's modulus, Poisson's ratio, and the density of the concrete deck are 34.5GPa, 0.2, and 2700 kg/m^3, respectively. The I-girder is 1.8 m in height with a section area of 854.4 cm^2. The top flange width and bottom flange width are 800 mm and 960 mm, respectively. The Young's modulus, Poisson's ratio, and the density of the I-girder are 206 GPa, 0.28, and 7850 kg/m^3, respectively.

In the finite element model, it is assumed that there is no relative slip between the I-beam girder and the concrete

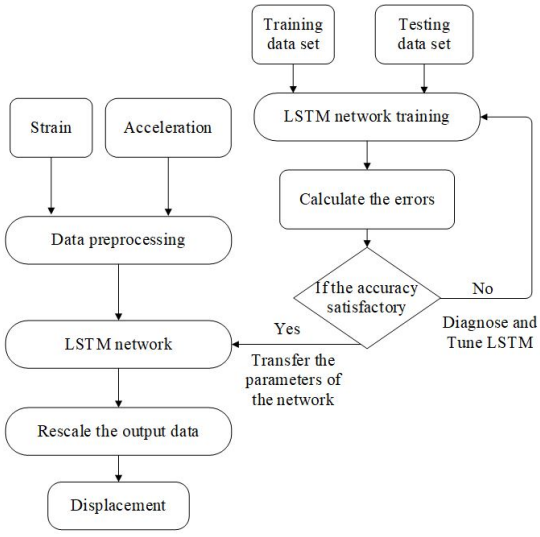

Fig. 3 The processes for displacement reconstruction

Fig. 4 The Shouchun Huaihe river bridge

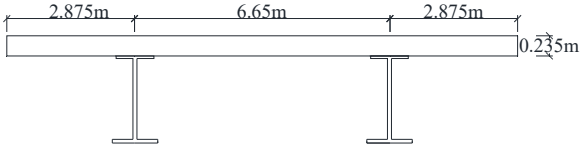

Fig. 5 The cross-section of the bridge

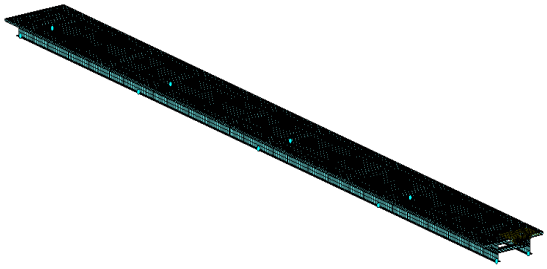

Fig. 6 The finite element model of the bridge

Table 1 The vehicle types

No.	Vehicle type	Vehicle axis model
V_1	Two-axle car	
V_2	Two-axle truck	
V_3	Six-axle trailer	

deck, and the two are rigidly connected. The whole bridge model is established using the software ANSYS, and the model contains 54780 nodes and 44080 elements. The Solid 185 elements are used to establish the concrete bridge deck, and Shell 181 elements are used to establish the I-beam and diaphragm. The overall finite element model of the bridge is shown in Fig. 6.

3.2 Stochastic vehicle flow and Vehicle model

The stochastic vehicle load is used for the vehicle-bridge coupled system simulation. The simulation of the stochastic traffic flow is based on the statistical data collected by the weight in motion system installed on the steel-composite girder bridge. In the 2020 survey of the traffic flow, the vehicle speed, the distance between two vehicles, and vehicle weight are collected while vehicles passing through the bridge. According to statistical data, three vehicle types classified as V_1, V_2, and V_3 listed in Table 1 are used to generate the stochastic traffic flow. V_1 is a two-axle car, V_2 is a three-axle truck, and V_3 is a six-axle trailer. The vehicle models composed of the vehicle body, wheelset, suspension, and shock absorber can fully simulate the actual movement of the vehicle.

In the statistics, the V_1 vehicles were 482,956 accounting for 49.0% of the total vehicles; V_2 vehicles totaled 163,845, accounting for 16.6% of the total vehicles; V_3 vehicles totaled 242797 accounting for 24.6% of the total vehicles, and the others account for 9.8%. The overall traffic volume is dominated by two-axle cars and six-axle trailers. The measured velocity of V1 basically follow Normal distribution with mean μ = 94.36 and standard deviation σ = 19.24, and the measured speed of V2 and V3 basically follow Normal distributions with $[\mu, \sigma]$ = [60.90, 10.34] and $[\mu, \sigma]$ = [65.83, 10.66], respectively. The vehicle

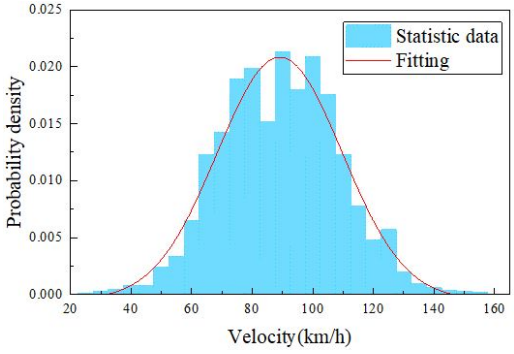

(a) The velocity distribution of V_1

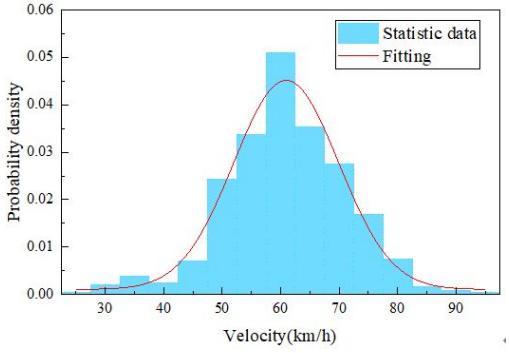

(b) The velocity distribution of V_2

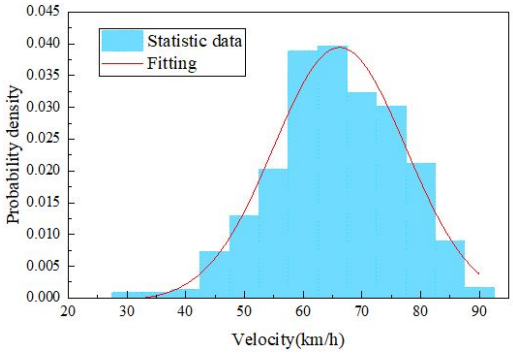

(c) The velocity distribution of V_3

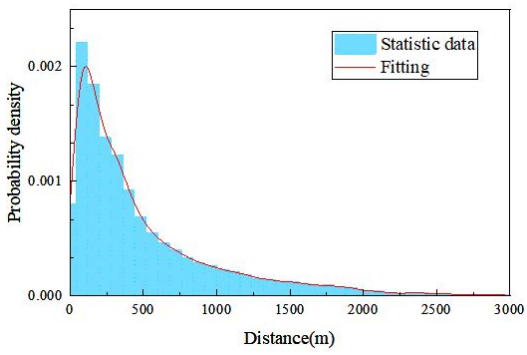

(d) The distribution of the distance between vehicles

Fig. 7 The statistical probability distributions of vehicles

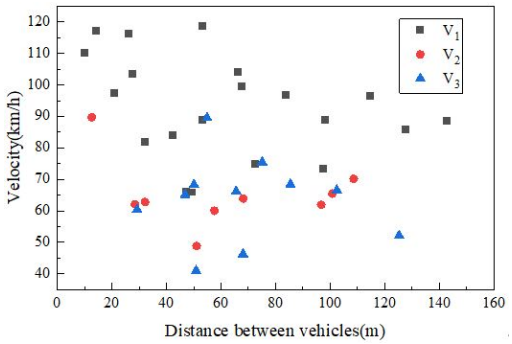

Fig. 8 The characteristics of the stochastic traffic flow in one lane

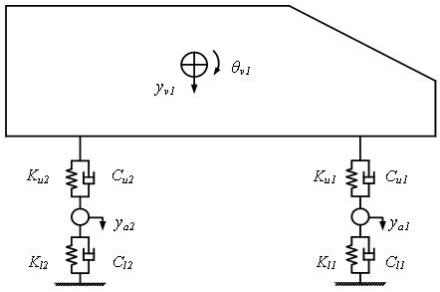

Fig. 9 The half-car model of the two-axle car

distance follows the logarithmic normal distribution with $[\mu, \sigma]$ = [5.81, 0.96]. According to the statistical results, the weight of V_1, V_2 and V_3 are set as 1.6 t, 20 t and 50 t respectively in the simulation. The statistical results are shown in Fig. 7. In the simulation, the stochastic traffic flow is generated based on the statistical probability distributions of the variables. For example, the characteristics of the generated stochastic traffic flow in one lane is given in Fig. 8.

The vehicle models are established by the software Universal Mechanism. Taking a two-axle vehicle V_1 as an example, the car body with vertical translation (y_{v1}) and vertical swing (θ_{v1}) is supported on the suspension system. Each suspension system is composed of a damper (C_{li}) and linear springs (K_{ui}, K_{li}) (I = 1,2). The vehicle model is shown in Fig. 9.

3.3 The calculated dynamic responses

The dynamic vehicle-bridge coupled system is simulated by the software Universal Mechanism using the bridge and vehicle models with the mass, stiffness and damping matrixes. The bridge model is supported by the rigid bodies, and the road roughness is considered. The vehicle-bridge coupled system is shown in Fig. 10.

The road roughness is set class-Normal of the ISO 8608 standard in the simulation. According to the ISO 8608 standard, the expression of road roughness can be obtained by inverse Fourier transform of power spectral density function as

$$r(x) = \sum_{k=1}^{N} \sqrt{2\varphi(n_k)\Delta n}\cos(2\pi n_k x + \theta_k). \quad (14)$$

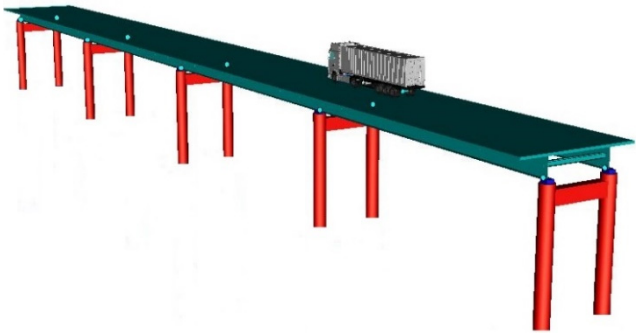

Fig. 10 The overall vehicle-bridge coupled system

where, φ is the power spectral density function for evaluating the roughness of road surface; n_k is the number of the wave; $\Delta n = 1/N\Delta$, N is the number of data points and Δ is the discrete distance interval; θ_k is the random phase angle uniformly distributed in a range of $[0,2\pi]$.

Based on the displacement and the interaction force relationship at the contact point between the bridge and the vehicle tire, the equation of motion for the vehicle-bridge coupling system combining with the motion equation of the bridge and the vehicle is established as (Deng and Cai 2010)

$$\begin{bmatrix} M_b & \\ & M_v \end{bmatrix}\begin{Bmatrix} \ddot{d}_b \\ \ddot{d}_v \end{Bmatrix} + \begin{bmatrix} C_b + C_{bb} & C_{bv} \\ C_{vb} & C_v \end{bmatrix}\begin{Bmatrix} \dot{d}_b \\ \dot{d}_v \end{Bmatrix} + \begin{bmatrix} K_b + K_{bb} & K_{bv} \\ K_{vb} & K_v \end{bmatrix}\begin{Bmatrix} d_b \\ d_v \end{Bmatrix} = \begin{Bmatrix} F_{br} \\ F_{vr} + F_G \end{Bmatrix} \quad (15)$$

where $[M_b]$, $[C_b]$ and $[K_b]$ are the mass, damping and stiffness matrixes of the bridge, respectively; $[M_v]$, $[C_v]$ and $[K_v]$ are the mass, damping, and stiffness matrixes of the vehicle, respectively; $\{d_b\}$ and $\{d_v\}$ are the displacement vector of the bridge and vehicle; $\{F_G\}$ is the gravity vector of the vehicle. C_{bb}, C_{bv}, C_{vb}, K_{bb}, K_{bv}, K_{vb} are the time-dependent terms due to the wheel–road contact forces. F_{br}, F_{vr} are the vehicle-bridge interaction force change as the vehicles move across the bridge. The time-dependent terms of the Eq. (15) are updated when the vehicles change the location in the simulation.

The strains, accelerations, and displacements at the measuring points are obtained by the simulation with the sampling rate of 100 Hz. The assumed arrangements of the measuring points are illustrated in Fig. 11. At 1/4, 1/2 and 3/4 of every span, the measuring points are arranged. The strain data are obtained from the 12 measuring points (N1~N12). The acceleration and reference displacement of points N2, N5, N8, and N11 are also obtained for the training and validation.

In the simulation, the dynamic responses of the vehicle-bridge coupled system due to the stochastic traffic flow are obtained. The data are collected for 20 minutes including the training set in the first 15 minutes and validation set in the last 5 minutes. There are 12 strain data channels, 4 acceleration data channels, and 4 displacement data channels in the train and validation data set. The LSTM network is trained and validated by the training and validation data set. The dynamic responses of N2 and N5 are shown in Fig. 12 for example.

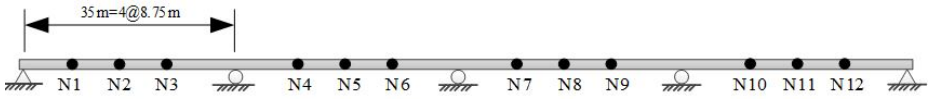

Fig. 11 The assumed arrangement of the measuring points

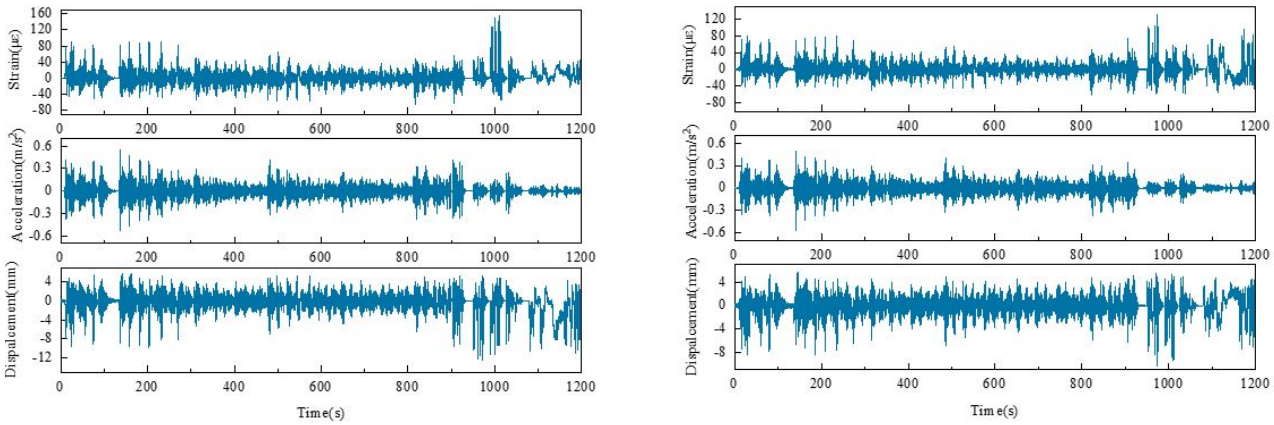

(a) At point N2 (b) At point N5

Fig. 12 The raw data obtain by the numerical simulation

4. LSTM network training

4.1 The training results of the LSTM network

To initialize the LSTM network for the displacement reconstruction, the collected training and validation data sets mentioned in section 3.3 are used to train the network model. The open-source platform TensorFlow is used to train the proposed LSTM network model in this study. The stochastic gradient descent method based on Adam algorithm is used to update the weights and other parameters of the model. The learning rate and the batch size are set as 0.0001 and 10, respectively. The LSTM network is built with 3 hidden layers and input length of 60.

After trials, the dimension of hidden state vectors is chosen to be 32. The epoch number defines the times that the algorithm will work. In the LSTM network training of this paper, all drop curves of the training RMSE get flat before 400 epochs.

The errors are calculated by Eqs. (11) and (12). The RMSEs of different points are presented in Fig. 13. According to the errors, the training and validation losses get close smoothly. The proposed LSTM network learns well from the training without underfitting and overfitting phenomena. The average RMSE and E are 0.0665 mm and 3.37%, respectively in training. In the validation, the average RMSE and E are 0.0985 mm and 4.89%.

The displacement of the validation data set is

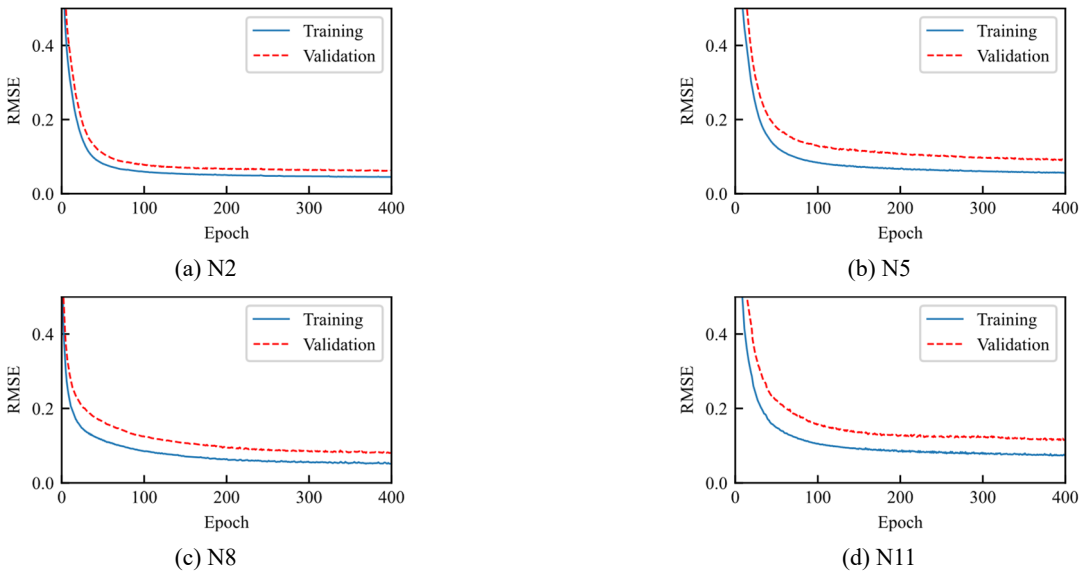

(a) N2 (b) N5

(c) N8 (d) N11

Fig. 13 The Training and validation errors of different points

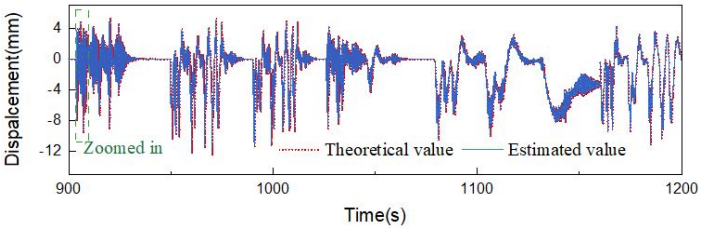

(a) Displacement reconstruction results of the validation

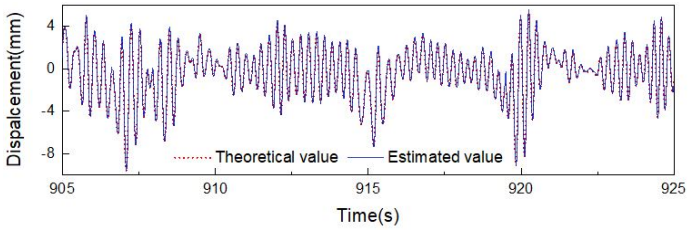

(b) The zoomed-in view of the first 20 seconds

Fig. 14 The displacement reconstruction of N2 in the validation

reconstructed, and the displacement of N2 is presented in Fig. 14(a) with the zoomed-in view of the first 20 seconds in Fig. 14(b). The proposed method can reconstruct the displacement accurately with maximum errors appearing at some peaks of the displacement.

4.2 Hyper-parameter study of LSTM network

The hyper-parameters such as the number of hidden layers, input length, batch size and dimension of hidden state vectors can influence the displacement reconstruction accuracy. To investigate the parameter effect of the LSTM networks, the networks with different hyper-parameters are compared. The number of hidden layers is set in the range of 1 to 4; the input length is set in the range of 30 to 120; the batch size is set in the range of 5 to 20, and the dimension of hidden state vectors is set in the range of 20 to 64. In Table 2, the performances of the LSTM networks are evaluated by the validation errors. The errors are calculated by Eqs. (11) and (12).

According to the results, though the training error may be decreased when making the network model more complicated, the accuracy in the validation cannot be improved by just increasing the number of hidden layers and state vectors. Besides, the training time is highly increased with the increment of the network complexity. The LSTM network model with 3 hidden layers is appropriate to reconstruct the dynamic displacement of the vehicle-bridge coupled system.

4.3 Comparison study of various networks

To verify the performance of the proposed LSTM network, different methods such as the support vector regression (SVR), RNN with three hidden layers, and LSTM network with three hidden layers are compared using the same training and validation data sets obtained in section 3.

The SVR model (Awad and Khanna 2015) has been used in regression problems. The regularization parameter

Table 2 Hyper-parameter study for the LSTM network model

No.	Hyper-parameters				Average errors	
	Number of hidden layers	Input length	Batch size	Dimension of hidden state vectors	RMSE (10^{-2}mm)	E (%)
1(origin)	3	60	10	32	9.85	4.89
2	3	60	10	64	10.36	5.14
3	3	60	10	20	10.31	5.11
4	3	60	20	32	10.72	5.32
5	3	60	5	32	10.25	5.08
6	3	120	10	32	10.21	5.06
7	3	30	10	32	10.57	5.24
8	1	60	10	32	10.92	5.42
9	2	60	10	32	10.20	5.06
10	4	60	10	32	10.26	5.09

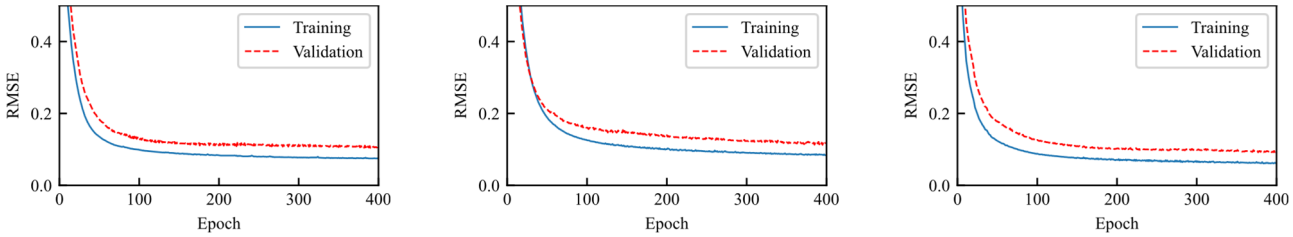

(a) SVR (b) RNN (c) LSTM

Fig. 15 Average errors for various models

Table 3 Errors for various method

Method	Average errors	
	RMSE (10^{-2} mm)	E (%)
SVR	10.95	5.43
RNN	11.88	5.63
LSTM	9.85	4.89

of the SVR network is set as 0.01 in this section. For the recurrent networks, the RNN layers or the LSTM layers contain 32 hidden state vectors in each layer. The performances of SVR, RNN and LSTM methods are compared by the error indexes of validation. The average RMSEs decreasing of all the estimation in 400 epochs of training processes are shown in Fig. 15.

According to the errors listed in Table 3, the RNN is of the lowest accuracy compared with the SVR and LSTM network, and the LSTM network is the most accurate among the three methods. The LSTM network has a relatively longer memory than RNN which is the reason that LSTM network performs better than the RNN. Though the learning curves of the SVR method are close to each other, the final accuracy of the validation is worse than the LSTM network.

5. Bridge displacement reconstruction

In this section, the performance of the trained LSTM network in section 4 is further tested with the load of a two-axle truck model with 55 t weight. The bridge model is the same as section 3.1, and the tested cases are the bridge under a single vehicle with various velocities and multiple vehicles. All the dynamic responses of the vehicle-bridge coupled system are calculated by the software Universal Mechanism. The measuring points of the bridge are shown in Fig. 11.

5.1 Displacement reconstruction due to single vehicle

To verify the proposed method, the displacement reconstruction results with various vehicle speeds are presented, and the strain-based only and acceleration-based only displacement reconstruction methods are used for comparison. The dynamic responses of the bridge are obtained when the truck drives through the bridge. With the vehicle speed of 40 km/h, the strain and acceleration responses at measuring point N2 are presented in Fig. 16. for example.

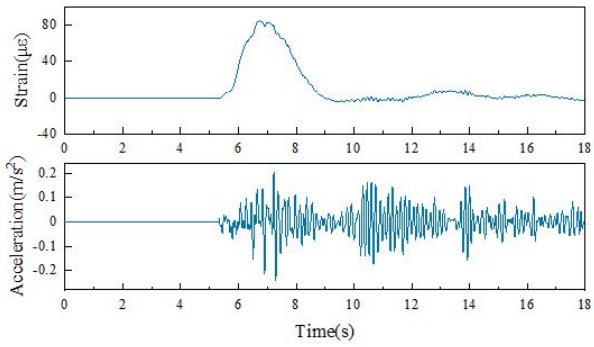

Fig. 16 The strain and acceleration responses at point N2

With the strain and acceleration data, the displacement is reconstructed by the LSTM network trained in section 4.1. The comparisons of the displacements reconstructed in different ways are shown in Figs. 17-19. The strain-based method reconstructs the dynamic displacements by the similar LSTM network as the data fusion method only with input strain data channels, and the acceleration-based method rebuilds the displacements with the FIR filter and the integration (Lee *et al*. 2010). The LSTM network is verified in three cases when the same truck drives through the bridge at different speeds. There are three load cases, and the speeds of the vehicle are 40 km/h, 60 km/h and 80 km/h, respectively. The dynamic displacement responses reconstructed by different methods are presented for comparison.

The acceleration-based method only needs the acceleration series at the target point. However, it is easy to cause low-frequency drift in displacement reconstruction. Though the strain-based displacement estimation can reconstruct the displacement well without knowing the neural axis and mode shapes by using the trained LSTM network, the high-frequency information may be lost due to the relative low-frequency sampling rate of the strain sensors. For the data fusion method, the acceleration and strain responses are used as input data to reconstruct the displacement with the trained LSTM network. The results indicate the data fusion method can achieve higher accuracy than the other two methods based on only strain or acceleration data. The LSTM network can reconstruct the displacement accurately without knowing the neutral axis and mode shapes.

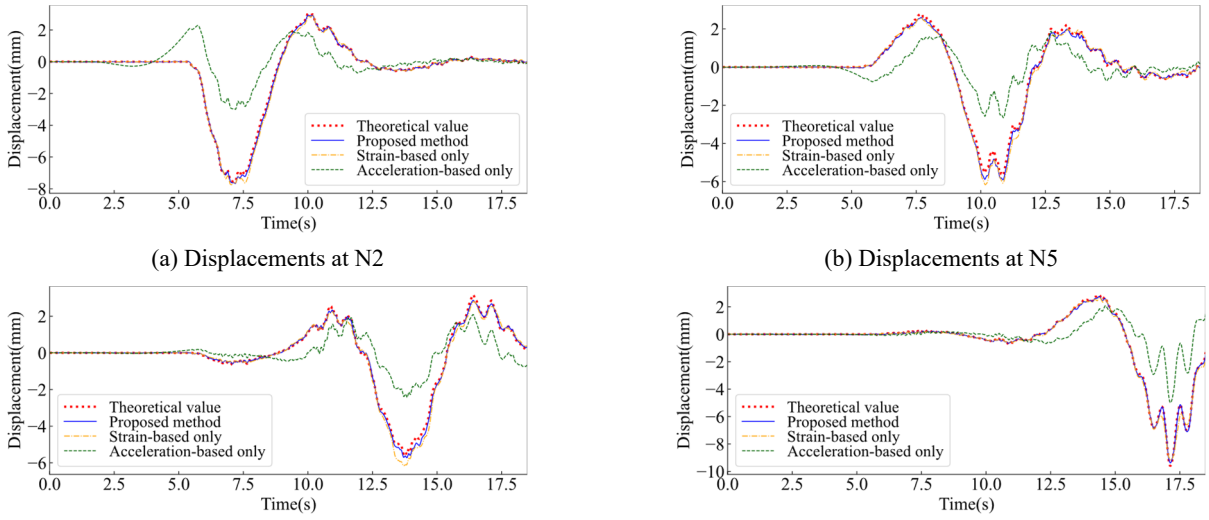

(a) Displacements at N2 (b) Displacements at N5

(c) Displacements at N8 (d) Displacements at N11

Fig. 17 Comparisons of the estimated displacements with the vehicle speed of 40 km/h

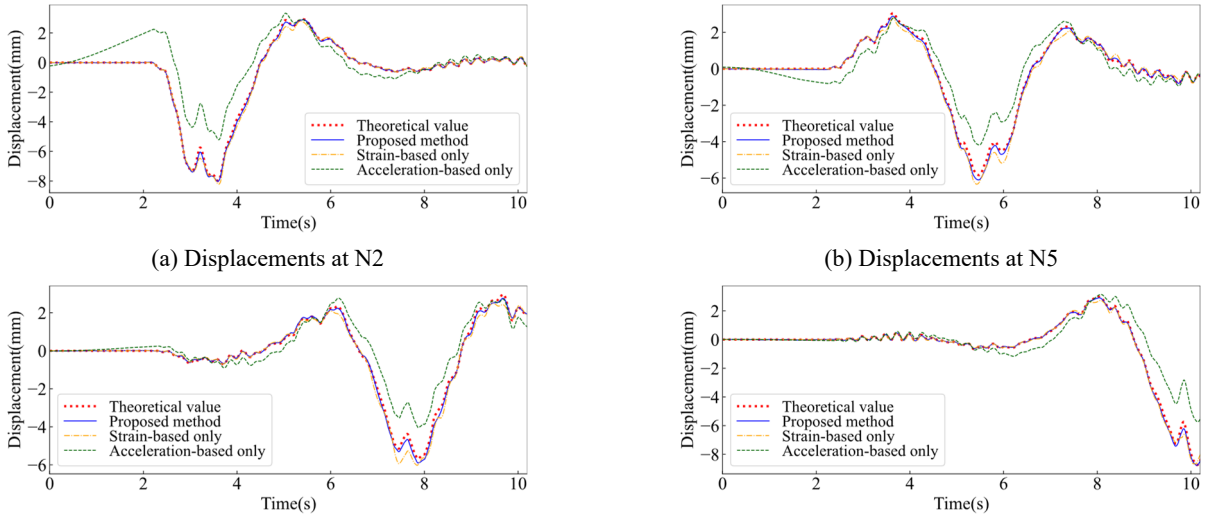

(a) Displacements at N2 (b) Displacements at N5

(c) Displacements at N8 (d) Displacements at N11

Fig. 18 Comparisons of the estimated displacements with the vehicle speed of 60 km/h

In the frequency domain, it is proved that both the high and low-frequency information are remained through the displacement reconstruction by the data fusion method. The comparisons of the displacements in the frequency domain are shown in Fig. 20. The power spectrums of the reference and the data fusion results are well matched. The errors of the different methods are calculated by Eq. (12) and listed in Table 4. The errors between the displacements estimated by the data fusion method and the reference displacements are below 9%.

Due to the measurement noise in the engineering application, it should be ensured that the proposed method is robust to the strain and acceleration measurement noise. Different levels of Gaussian white noise are added to the input strain and acceleration responses for the vehicle speed of 40 km/h, and the corresponding displacements are generated by the same LSTM network. The noise-signal ratio (SNR) is defined as Eq. (16) to describe the additive noise level.

$$NSR = \frac{P_{noise}}{P_{signal}} \tag{16}$$

where P_{noise} and P_{signal} are the average power of the noise and signal respectively.

The displacement reconstruction results are compared in Fig. 21, and the error indexes are listed in Table 5. Though errors increase slightly with the c of the input data noise level, the results indicate that the error increase is less than 1.4% with the noise-to-signal ratio of 10% additive Gaussian noise in the input data. The LSTM network model works well when the input strain and acceleration data are added with noise-to-signal ratio of 5% Gaussian noise. To simulate the measuring error, the input strain and acceleration responses are applied with 5% Gaussian noise in the rest of the numerical simulation section.

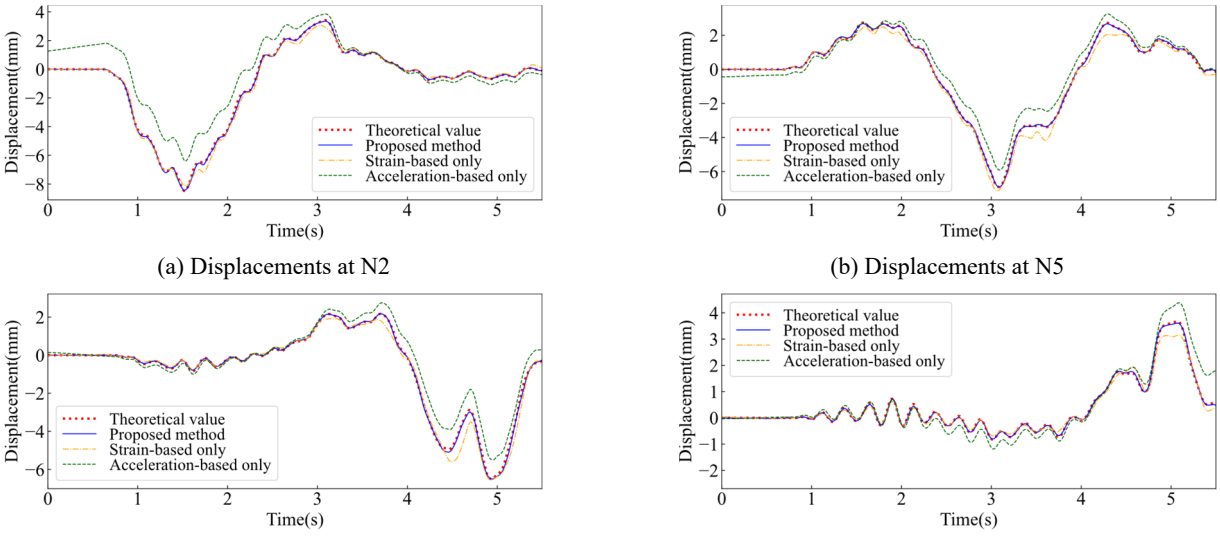

(a) Displacements at N2

(b) Displacements at N5

(c) Displacements at N8

(d) Displacements at N11

Fig. 19 Comparisons of the estimated displacements with the vehicle speed of 80 km/h

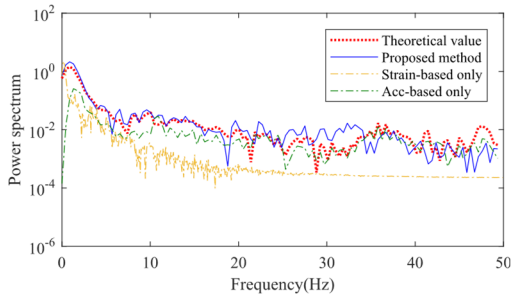

Fig. 20 Comparison of displacements in the frequency domain

Table 4 Errors at main points with different vehicle speed

Vehicle speed	Point	Error index E (%)		
		Proposed method	Strain-based only	Acceleration-based only
40 km/h	N2	6.31	9.73	53.47
	N5	8.94	14.15	40.90
	N8	8.75	14.24	36.19
	N11	5.46	11.37	56.30
60 km/h	N2	4.90	10.62	46.60
	N5	7.13	14.27	24.89
	N8	8.29	16.62	23.84
	N11	8.32	10.24	35.68
80 km/h	N2	4.73	12.29	35.99
	N5	3.66	14.27	24.89
	N8	4.42	26.13	25.13
	N11	5.10	7.81	12.30

Table 5 Errors of different measuring points with noise effect

Point	Error index E (%)		
	No noise	5% noise	10% noise
N2	6.31	6.65	7.67
N5	8.94	9.14	9.53
N8	8.75	8.81	9.87
N11	5.46	5.72	5.53

5.2 Displacement reconstruction due to multiple vehicles

The displacements of the bridge are reconstructed while multiple vehicles drive through the bridge. In this case, three trucks weighted 55 t drive through the bridge with the speed of 60 km/h. The distance between the trucks is 35 m. Under the load of three trucks, the strain and acceleration responses of measuring point N2 are shown in Fig. 22.

The comparisons of the reconstructed displacements and the references are shown in Fig. 23. The results of the displacement reconstruction indicate that the proposed method is of ideal applicability and accuracy. The error of displacements converted by the FIR filter is huge because the filter eliminates the low-frequency information of the input data to avoid low-frequency drift. As listed in table 6, the proposed method is accurate in this case with a load of multiple vehicles. The maximum of errors is below 7.5%. The accuracy of the data fusion method is improved comparing with the strain-based only method according to the additional acceleration data. The LSTM network works well in different situations. From the comparisons of the estimated results and the errors in different cases, it is indicated that the data fusion method can achieve higher accuracy.

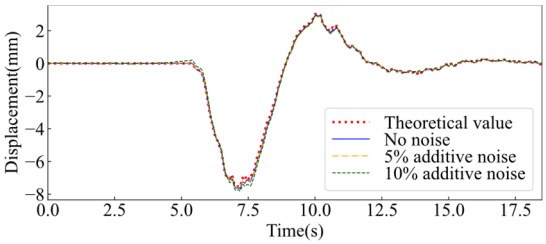

(a) Displacements at N2

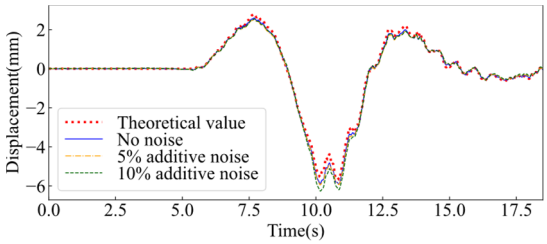

(b) Displacements at N5

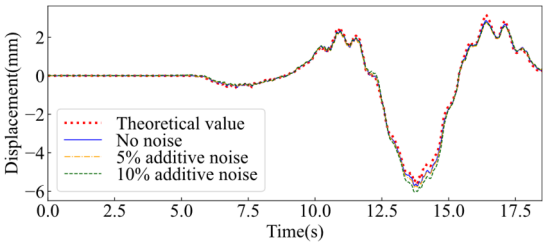

(c) Displacements at N8

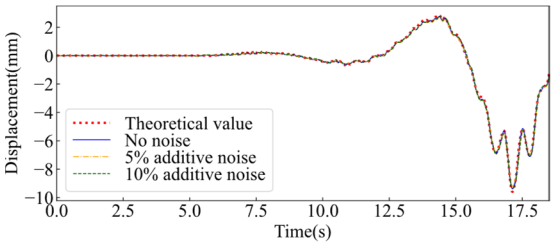

(d) Displacements at N11

Fig. 21 Comparisons of the estimated displacements with noise effect

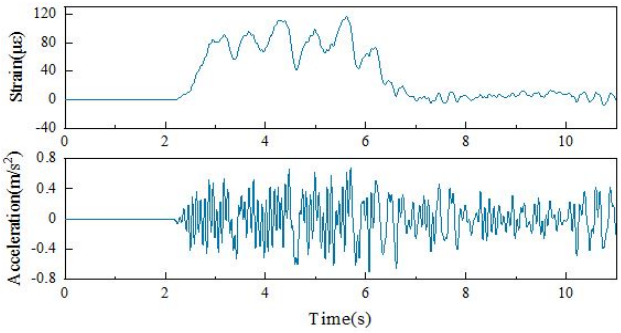

Fig. 22 The strain and acceleration responses at point N2

Table 6 Errors of different measuring points for the multiple vehicles load case

Point	Error index E (%)		
	Proposed method	Strain-based only	Acceleration-based only
N2	7.50	13.05	96.67
N5	5.45	7.14	43.53
N8	4.13	5.41	44.37
N11	3.98	4.44	36.53

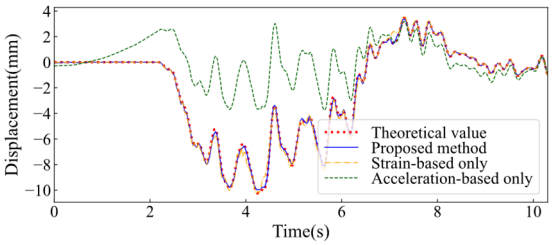

(a) Displacements at N2

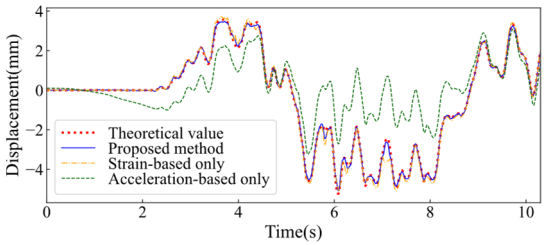

(b) Displacements at N5

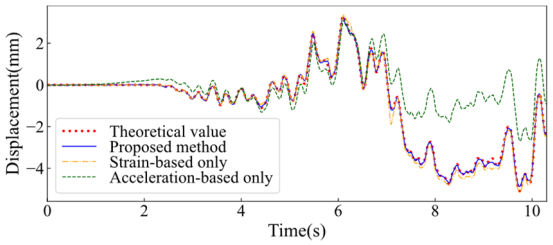

(c) Displacements at N8

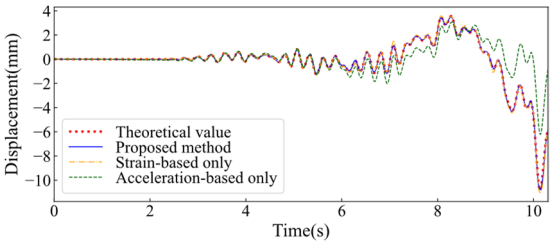

(d) Displacements at N11

Fig. 23 Comparisons of the estimated displacements due to multiple vehicles

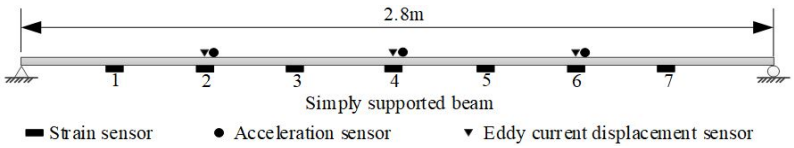

Fig. 24 The sensor arrangement of the tested simply supported beam

Fig. 25 The overall placement of the tested beam

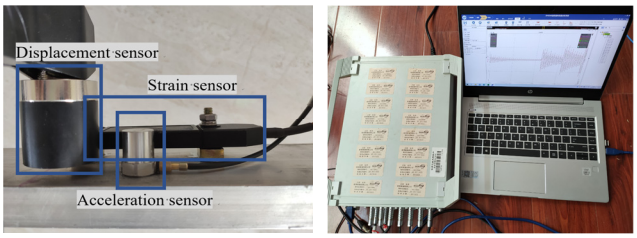

Fig. 26 The sensors and the signal acquisition system

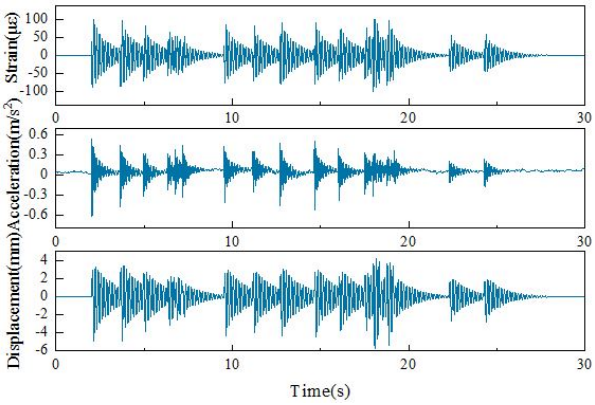

Fig. 27 The training data at measurement point 4

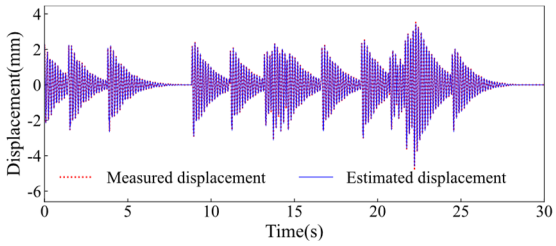

Fig. 28 The estimation of measuring point 4

6. Experimental verification

In the experimental verification, the responses of a simply supported beam and a two-span continuous beam are obtained in the laboratory. To verify the proposed method, multi-point random hammering excitation is chosen to provide high and low-frequency excitation. The tested beams are aluminum beams of 2.8 m in length. The width and the thickness of the test beams are 100 mm and 20 mm respectively. The Young's modulus, Poisson's ratio and the density of the beam are 70 GPa, 0.33, and 2700 kg/m^3, respectively.

6.1 Displacement reconstruction for the simply supported beam

For the simply supported beam, seven strain sensors are placed on the beam surface uniformly with an interval of 35 cm. At the 1/4, 1/2 and 3/4 span, the acceleration sensors and eddy current displacement sensors are installed. The sensor arrangement of the simply supported beam is shown in Fig. 24. The overall experiment placement is illustrated in Fig. 25, and the sensors and the signal acquisition system are shown in Fig. 26. The strains, accelerations and displacements are all measured with the sampling frequency of 200 kHz.

With the random hammering excitation, the strains, accelerations and displacements are obtained at the same time by the signal acquisition system. The LSTM network with 10 input channels and 3 output channels is established. The learning rate and the batch size are set as 0.0001 and 10, respectively. The LSTM network is built with 3 hidden layers and input length of 60. The dimension of hidden state vectors is chosen to be 64 and the training epoch is set to 400. The 30 seconds of the responses are set as training data, and the data of the measuring point 4 is shown in Fig. 27. for example.

The first case is the displacement reconstruction due to single hammering random excitation. After training, the dynamic displacements due to single hammering random excitation are reconstructed for 30 seconds. In Fig. 28. the displacement reconstruction of point 4 with the random single hammering excitation are presented. To clearly show the displacement reconstruction results, the comparison of the measured displacements and the displacements reconstructed by the proposed methods in the first 3 seconds are shown in Fig. 29.

The errors between the estimated displacements and the measured displacements are shown in Fig. 30. The errors are calculated every 5 seconds by Eq. (12). The maximum error of the estimation is less than 6% in 3 measuring points. With the larger displacement at the mid-span of the beam, the estimation errors at point 4 are relatively larger than that of the other two measuring points.

Then the proposed methods are verified with multiple hammering random excitations. Total 30 seconds of the dynamic displacements are estimated by the trained LSTM

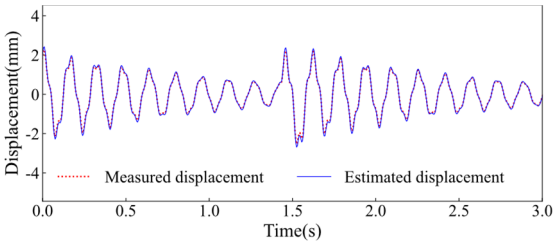

(a) Displacements at point 2

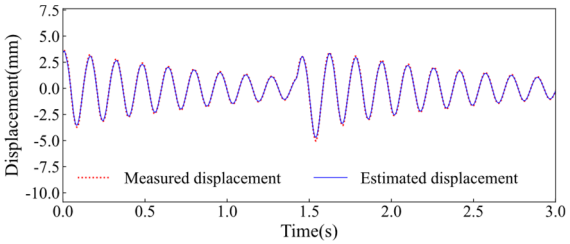

(b) Displacements at point 4

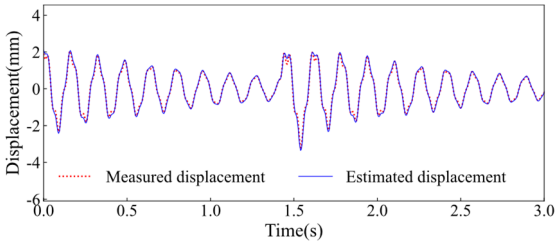

(c) Displacements at point 6

Fig. 29 Displacements reconstruction results of the tested simply supported beam

network. The displacement reconstruction results of the first 3 seconds are shown in Fig. 31, and the errors calculated every 5 seconds are shown in Fig. 32. In this case, all the estimation errors are below 6%, and the errors at the mid-span are the largest among the three measuring points.

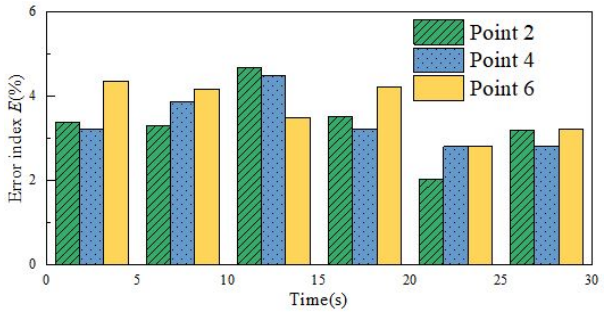

Fig. 30 The displacement reconstruction errors of the tested simply supported beam

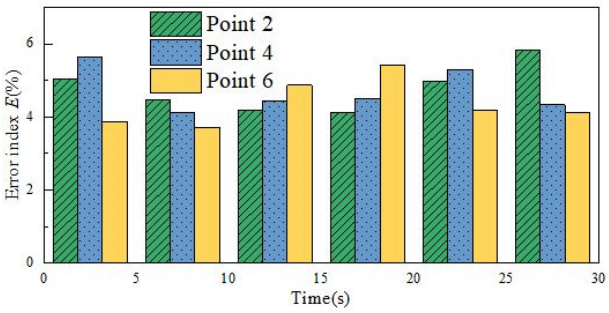

Fig. 32 The displacement reconstruction errors of the tested simply supported beam

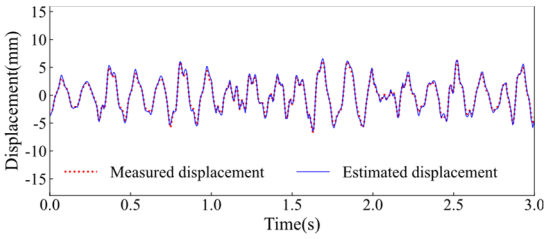

(a) Displacements at point 2

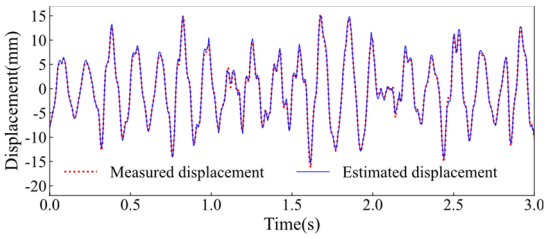

(b) Displacements at point 4

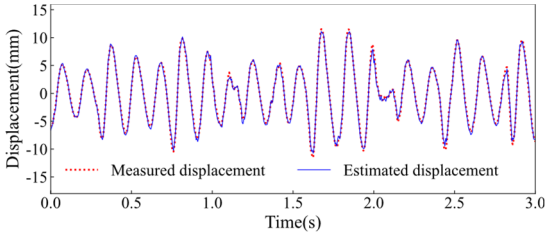

(c) Displacements at point 6

Fig. 31 Comparisons of the estimated displacements of the tested simply supported beam

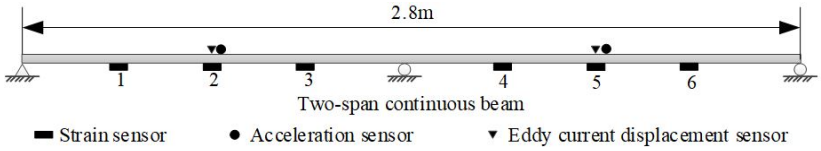

Fig. 33 The sensor arrangement of the tested two-span continuous beam

Fig. 34 The overall placement of the tested two-span continuous beam

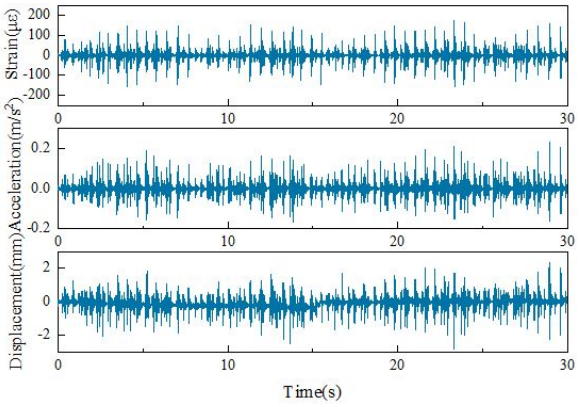

Fig. 35 The responses of point 2 in the training data set

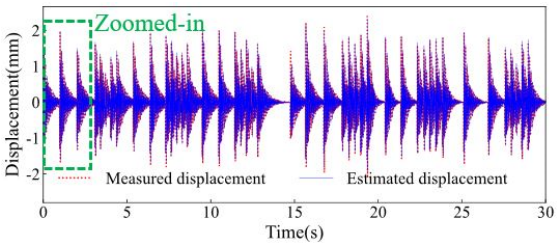

Fig. 36 The estimation of measuring point 2

6.2 Displacement reconstruction for the two-span continuous beam

As for the two-span continuous beam, the sensor arrangement is shown in Fig. 33, and the overall experiment placement of the test is illustrated in Fig. 34. The span length is 1.4m. The tested beam and the signal acquisition system are the same as the simply supported beam. An LSTM network with 8 input channels and 2 output channels is established. The learning rate and the batch size are set as 0.0001 and 10, respectively. The LSTM network is built with 3 hidden layers and input length of 60. The dimension of hidden state vectors is chosen to be 32 and the training epoch is set to 400.

The displacements due to the hammering random excitation at points 2 and 5 are reconstructed by the stacked LSTM network. Under multiple hammering excitation, the dynamic responses within 30 seconds of the continuous beam are set as the training set to initialize the LSTM network. The LSTM model contains a similar structure with three hidden layers and 8 input channels and 2 output channels. The 30 seconds of the responses are set as training data, and the data of the measuring point 2 is shown in Fig. 35 for example.

Again, for the first case, single hammering random excitation is given to the continuous beam. The dynamic displacements are reconstructed for 30 seconds. The displacement reconstruction results of point 2 are shown in Fig. 36, and the first 3 seconds of the estimated displacements are illustrated in Fig. 37. The curves of the estimated displacement fit the measurements well. In Fig. 38, the errors of the estimated and reference displacements are calculated every 5 seconds, and the maximum error is below 6%.

For the second case, the dynamic displacement responses of the continuous beam under multiple hammering excitations are estimated by the same LSTM network. The estimated displacements in the first 3 seconds

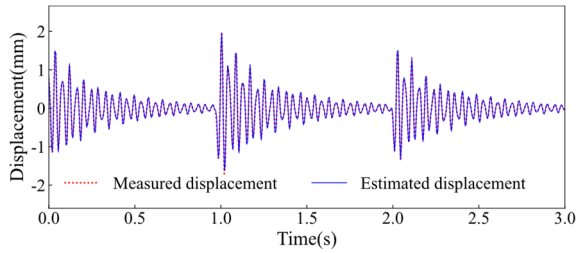

(a) Displacements at point 2

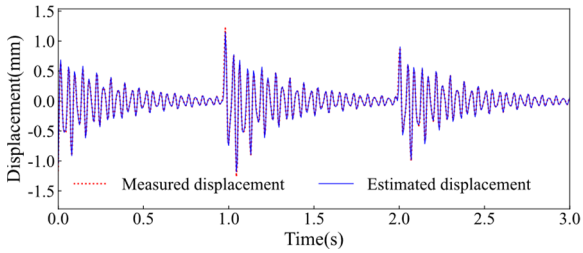

(b) Displacements at point 4

Fig. 37 Comparisons of the estimated displacements for the two-span continuous beam

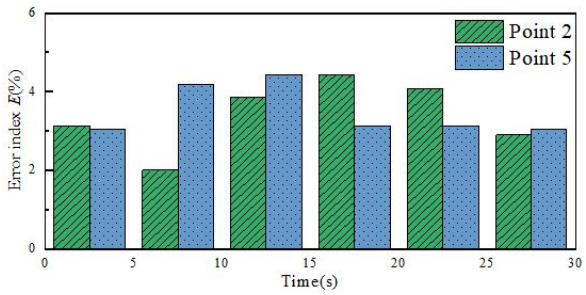

Fig. 38 The displacement reconstruction errors of the tested two-span continuous beam

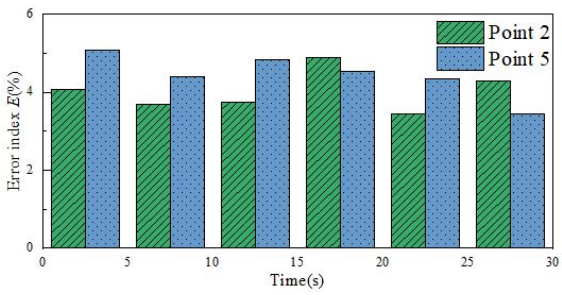

Fig. 40 The displacement reconstruction errors of the tested two-span continuous beam

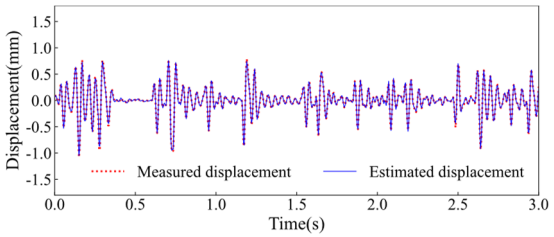

(a) Displacements at point 2

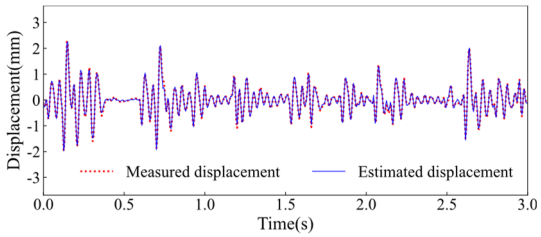

(b) Displacements at point 5

Fig. 39 Comparisons of the estimated displacements of the tested two-span continuous beam

are illustrated in Fig. 39, and the errors of the estimation in every 5 seconds are shown in Fig. 40. In the experiment, the maximum error of the proposed method is below 6%, and the LSTM networks perform steadily in different cases. The errors of the cases with single hammering excitation are relatively lower than that of the cases with multiple hammering excitations.

7. Conclusions

In this paper, a displacement reconstruction method based on the LSTM networks is proposed. The proposed method can fuse the measured acceleration and strain data, to achieve the displacement reconstruction with high accuracy. The stacked LSTM layers in the network model can increase the depth of the network and make the artificial neural network able to learn the complicated relationships between different kinds of data. The proposed method is verified by the simulation and experiment, and the networks perform well in different load cases. The main conclusions can be drawn as follows:

- Both the numerical and experimental results indicate the proposed displacement reconstruction method based on LSTM networks can achieve dynamic displacement reconstruction.
- With the strain and acceleration data as input, the trained LSTM networks can make the displacement reconstruction more accurate than the methods based on strain or acceleration only. The LSTM networks can estimate the displacements accurately in different load cases, and it is also robust to the measuring noise.
- The accuracy of the LSTM network with three hidden layers is more accurate comparing with the SVR, RNN and single-layer LSTM networks.

Acknowledgments

Financial support to complete this study was provided in part by the National Natural Science Foundation of China under grand Nos. 51922036, by the key research and development project of Anhui province under grand No. 1804a0802204, by The Fundamental Research Funds for the Central Universities under grand No. JZ2020HGPB0117, and by the Natural Science Funds for Distinguished Young Scholar of Anhui province under grand No.1708085J06. The results and opinions expressed in this paper are those of the authors only and they don't necessarily represent those of the sponsors.

References

Awad, M. and Khanna, R. (2015), "Support Vector Regression", In: *Efficient Learning Machines*: *Theories*, *Concepts*, *and Applications for Engineers and System Designers*, pp. 67-80. https://doi.org/10.1007/978-1-4302-5990-9_4

Candon, M.J., Esposito, M., Levinski, O., Joseph, N., Koschel, S., Carrese, R. and Marzocca, P. (2020), "On the Application of a Long-Short-Term Memory Deep Learning Architecture for Aircraft Transonic Buffet Loads Monitoring", *AIAA Scitech 2020 Forum*, 0702. https://doi.org/https://doi.org/10.2514/6.2020-0702

Cho, S., Yun, C.-B. and Sim, S.-H. (2015), "Displacement estimation of bridge structures using data fusion of acceleration and strain measurement incorporating finite element model", *Smart Struct. Syst., Int. J.*, **15**(3-4), 645-663. https://doi.org/10.12989/sss.2015.15.3.645

Chung, W., Kim, S., Kim, N.S. and Lee, H.U. (2008), "Deflection

estimation of a full scale prestressed concrete girder using long-gauge fiber optic sensors", *Constr. Build. Mater.*, **22**(3), 394-401. https://doi.org/10.1016/j.conbuildmat.2006.08.007

Deng, L. and Cai, C.S. (2010), "Development of dynamic impact factor for performance evaluation of existing multi-girder concrete bridges", *Eng. Struct.*, **32**(1), 21-31. https://doi.org/https://doi.org/10.1016/j.engstruct.2009.08.013

Fan, G., Li, J. and Hao, H. (2019), "Lost data recovery for structural health monitoring based on convolutional neural networks", *Struct. Control Health Monitor.*, **26**(10), e2433. https://doi.org/10.1002/stc.2433

Fan, G., Li, J. and Hao, H. (2020), "Dynamic response reconstruction for structural health monitoring using densely connected convolutional networks", *Struct. Health Monitor.*, **20**(4), 1373-1391. https://doi.org/10.1177/1475921720916881

Fan, G., Li, J., Hao, H. and Xin, Y. (2021), "Data driven structural dynamic response reconstruction using segment based generative adversarial networks", *Eng. Struct.*, **234**, 111970. https://doi.org/10.1016/j.engstruct.2021.111970

Glaser, R., Caccese, V. and Shahinpoor, M. (2012), "Shape monitoring of a beam structure from measured strain or curvature", *Exp. Mech.*, **52**(6), 591-606. https://doi.org/10.1007/s11340-011-9523-y

Graves, A. (2012), *Long Short-term Memory*, Springer, Berlin, Heidelberg, Germany.

Halil, H., Kim, D., Nam, J. and Park, K. (2016), "Accuracy and noise analyses of 3D vibration measurements using laser Doppler vibrometer", *Measurement*, **94**, 883-892. https://doi.org/10.1016/j.measurement.2016.09.003

Hester, D., Brownjohn, J., Bocian, M. and Xu, Y. (2017), "Low cost bridge load test: Calculating bridge displacement from acceleration for load assessment calculations", *Eng. Struct.*, **143**, 358-374. https://doi.org/https://doi.org/10.1016/j.engstruct.2017.04.021

Hoag, A., Hoult, N.A., Take, W.A., Moreu, F., Le, H. and Tolikonda, V. (2017), "Measuring displacements of a railroad bridge using DIC and accelerometers", *Smart Struct. Syst.*, *Int. J.*, **19**(2), 225-236. https://doi.org/10.12989/sss.2017.19.2.225

Hochreiter, S. and Schmidhuber, J. (1997), "Long short-term memory", *Neural Computat.*, **9**(8), 1735-1780.

Jang, S., Jo, H., Cho, S., Mechitov, K., Rice, J.A., Sim, S.-H., Jung, H.-J., Yun, C.-B., Spencer Jr., B.F. and Agha, G. (2010), "Structural health monitoring of a cable-stayed bridge using smart sensor technology: deployment and evaluation", *Smart Struct. Syst.*, *Int. J.*, **6**(5-6), 439-459. https://doi.org/10.12989/sss.2010.6.5_6.439

Kang, L.H., Kim, D.K. and Han, J.H. (2007), "Estimation of dynamic structural displacements using fiber Bragg grating strain sensors", *J. Sound Vib.*, **305**(3), 534-542. https://doi.org/10.1016/j.jsv.2007.04.037

Karim, F., Majumdar, S., Darabi, H. and Harford, S. (2019), "Multivariate LSTM-FCNs for time series classification", *Neural Networks*, **116**, 237-245. https://doi.org/10.1016/j.neunet.2019.04.014

Kim, H.I., Kang, L.H. and Han, J.H. (2011), "Shape estimation with distributed fiber Bragg grating sensors for rotating structures", *Smart Mater. Struct.*, **20**(3). https://doi.org/10.1088/0964-1726/20/3/035011

Kim, K., Choi, J., Chung, J., Koo, G., Bae, I.H. and Sohn, H. (2018), "Structural displacement estimation through multi-rate fusion of accelerometer and RTK-GPS displacement and velocity measurements", *Measurement*, **130**, 223-235. https://doi.org/10.1016/j.measurement.2018.07.090

Kingma, D.P. and Ba, J. (2014), Adam: A method for stochastic optimization, arXiv preprint arXiv:14126980.

Lee, H.S., Hong, Y.H. and Park, H.W. (2010), "Design of an FIR filter for the displacement reconstruction using measured acceleration in low-frequency dominant structures", *Int. J. Numer. Meth. Eng.*, **82**(4), 403-434. https://doi.org/10.1002/nme.2769

Lee, J., Lee, K.C., Lee, S., Lee, Y.J. and Sim, S.H. (2019), "Long-term displacement measurement of bridges using a LiDAR system", *Struct. Control Health Monitor.*, **26**(10). https://doi.org/10.1002/stc.2428

Lei, Y., Liu, C., Jiang, Y. and Mao, Y. (2013), "Substructure based structural damage detection with limited input and output measurements", *Smart Struct. Syst.*, *Int. J.*, **12**(6), 619-640. https://doi.org/10.12989/sss.2013.12.6.619

Li, S., Wang, X., Liu, H., Zhuo, Y., Su, W. and Di, H. (2020), "Dynamic deflection monitoring of high-speed railway bridges with the optimal inclinometer sensor placement", *Smart Struct. Syst.*, *Int. J.*, **26**(5), 591-603. https://doi.org/10.12989/sss.2020.26.5.591

Liu, L.J., Zhu, J.J., Su, Y. and Lei, Y. (2016), "Improved Kalman filter with unknown inputs based on data fusion of partial acceleration and displacement measurements", *Smart Struct. Syst.*, *Int. J.*, **17**(6), 903-915. https://doi.org/10.12989/sss.2016.17.6.903

Ma, Z., Chung, J., Liu, P. and Sohn, H. (2021), "Bridge displacement estimation by fusing accelerometer and strain gauge measurements", *Struct. Control Health Monitor.*, **28**(6). https://doi.org/10.1002/stc.2733

Moon, H.S., Ok, S., Chun, P.J. and Lim, Y.M. (2019), "ArtArtificial neural network for vertical displacement prediction of a bridge from strains (Part 1): Girder bridge under moving vehicles", *Appl. Sci.-Basel*, **9**(14). https://doi.org/10.3390/app9142881

Moreu, F., Jo, H., Li, J., Kim, R.E., Cho, S., Kimmle, A., Scola, S., Le, H., Spencer Jr., B.F. and Lafave, J.M. (2015), "Dynamic assessment of timber railroad bridges using displacements", *J. Bridge Eng.*, **20**(10). https://doi.org/10.1061/(Asce)Be.1943-5592.0000726

Moschas, F. and Stiros, S. (2011), "Measurement of the dynamic displacements and of the modal frequencies of a short-span pedestrian bridge using GPS and an accelerometer", *Eng. Struct.*, **33**(1), 10-17. https://doi.org/10.1016/j.engstruct.2010.09.013

Ni, Y.Q., Wang, Y.W., Liao, W.Y. and Chen, W.H. (2019), "A vision-based system for long-distance remote monitoring of dynamic displacement: experimental verification on a supertall structure", *Smart Struct. Syst.*, *Int. J.*, **24**(6), 769-781. https://doi.org/10.12989/sss.2019.24.6.769

Rapp, S., Kang, L.H., Han, J.H., Mueller, U.C. and Baier, H. (2009), "Displacement field estimation for a two-dimensional structure using fiber Bragg grating sensors", *Smart Mater. Struct.*, **18**(2). https://doi.org/10.1088/0964-1726/18/2/025006

Smyth, A. and Wu, M. (2007), "Multi-rate Kalman filtering for the data fusion of displacement and acceleration response measurements in dynamic system monitoring", *Mech. Syst. Signal Process.*, **21**(2), 706-723. https://doi.org/10.1016/j.ymssp.2006.03.005

Thong, Y.K., Woolfson, M.S., Crowe, J.A., Hayes-Gill, B.R. and Jones, D.A. (2004), "Numerical double integration of acceleration measurements in noise", *Measurement*, **36**(1), 73-92. https://doi.org/10.1016/j.measurement.2004.04.005

Tian, Y., Xu, Y., Zhang, D. and Li, H. (2020), "Relationship modeling between vehicle-induced girder vertical deflection and cable tension by BiLSTM using field monitoring data of a cable-stayed bridge", *Struct. Control Health Monitor.*, e2667. https://doi.org/10.1002/stc.2667

Yi, T.H., Li, H.N. and Gu, M. (2013), "Experimental assessment of high-rate GPS receivers for deformation monitoring of bridge", *Measurement*, **46**(1), 420-432. https://doi.org/10.1016/j.measurement.2012.07.018

Zheng, Z.P., Qiu, H., Wang, Z.C., Luo, S.J. and Lei, Y. (2019), "Data fusion based multi-rate Kalman filtering with unknown input for on-line estimation of dynamic displacements", *Measurement*, **131**, 211-218. https://doi.org/10.1016/j.measurement.2018.08.057

BS